Compact Mach-Zehnder Interferometer for Practical Vernier Effect Sensing System With High Extinction Ratio

Maolin Dai, *Graduate Student Member, IEEE*, Xuanyi Liu, Zhenmin Chen, *Member, IEEE*, Yuanfang Zhao, M. S. Aruna Gandhi, *Member, IEEE*, Qian Li, *Senior Member, IEEE*, and H. Y. Fu, *Senior Member, IEEE*

***Abstract*— Recently, Vernier effect is introduced into fiber optic interferometric sensors to enhance the sensitivity. To achieve a high-quality of the Vernier spectrum, the match of the free spectral range (FSR) and the extinction ratio (ER) in two arms is required. Furthermore, the reference arm should be designed to be different from the sensing arm to avoid crosstalk. In this work, a compact in-line Mach-Zehnder interferometer (MZI) by sandwiching a hollow capillary fiber (HCF) between two sections of no-core fiber (NCF) is proposed for the reference arm in Vernier effect based sensing system. FSR of the in-line MZI can be tuned by modulating the length of the HCF, while the ER can remain high up to ∼20 dB, which is equivalent to that of the polarization-maintaining fiber (PMF) based interferometers. Experimental results show that the MZI exhibits low sensitivity to temperature, strain, refractive index (RI) and torsion. When employed as the reference arm cascaded with PMF Sagnac interferometer (SI), the upper and lower envelope are with high extinction ratio (ER). The proposed MZI is a promising candidate for the reference arm in Vernier effect based sensing system with the merits of compact size, good spectral characteristics and insensitivity to ambient environment.**

***Index Terms*—Optical fiber sensors, mach-zehnder interferometers, vernier effect.**

I. Introduction

FIBER optic sensors have been intensively investigated as a powerful tool for measuring various parameters including physical and biochemical parameters with the merits of compact size, electromagnetic immunity, high sensitivity, fast response, and long-distance capability. For the point-type fiber optic sensors, they are mainly based on fiber gratings, resonances and fiber interferometers. Fiber interferometers, including Fabry-Perot interferometer (FPI) [1]–[3], Mach-Zehnder interferometer (MZI) [4]–[6], Michelson interferometer (MI) [7]–[9] and Sagnac interferometer (SI) [10], [11], are intensively developed to be the versatile sensing elements. The interferometer exhibits a highly periodic interferometric spectrum in the wavelength domain, which is like a ruler to measure the dip wavelength shift under ambient disturbances.

Inspired from Vernier calipers, Vernier effect is introduced into silicon photonic devices and fiber optic interferometers to modulate the wavelength output with improved sensing performance [12]–[15]. According to the principle of photonic Vernier effect in fiber interferometers, the smaller difference in free spectral ranges (FSRs) between reference arm and sensing arm, the higher sensitivity amplification can be achieved. Also, the smaller FSRs of the two arms, the higher spectral fineness can be obtained, which increases the demodulation accuracy.

To generate high-quality Vernier effect, the match between the extinction ratios (ERs) of two interferometric spectra is required. Therefore, many works use the same structure in both reference arm and sensing arm to achieve the high-quality Vernier spectrum, especially in polarization maintaining fiber (PMF) based schemes [13], [16]–[20]. The PMF based SI and Lyot filter exhibit a high fringe visibility due to their good transmission of two orthogonal modes, which is hard to be matched by other fiber interferometers, such as FPI [16], [18], [21], [22]. Although the sensing systems based on two sections of PMFs own good spectral characteristics, the long length of PMF makes the sensor bulky, which limits their application scenarios. Moreover, the same structure in both reference arm and sensing arm leads to their same sensitivities towards ambient variations. Under this condition, the reference arm should be well isolated from ambient environment, which hinders the device for practical applications.

To solve this issue, we utilize an MZI based on hybrid splicing of no-core fiber (NCF) and hollow capillary fiber (HCF). The highly-periodic interferometric spectrum with high ER and the insensitivity to temperature, strain, refractive index (RI) and

Manuscript received March 24, 2022; revised May 24, 2022; accepted May 30, 2022. Date of publication June 2, 2022; date of current version June 9, 2022. This work was supported in part by the Science, Technology and Innovation Commission of Shenzhen Municipality under Grant JCYJ20180507183815699 and in part by the Innovation Group Project of Southern Marine Science and Engineering Guangdong Laboratory under Grant 311021011. *(Corresponding author: H. Y. Fu.)*

Maolin Dai, Xuanyi Liu, and Yuanfang Zhao are with the Tsinghua-Berkeley Shenzhen Institute & Tsinghua Shenzhen International Graduate School, Tsinghua University, Shenzhen 518055, China (e-mail: dml19@mails.tsinghua.edu.cn; liuxuany20@mails.tsinghua.edu.cn; zhaoyf19@mails.tsinghua.edu.cn).

Zhenmin Chen is with Peng Cheng Laboratory, Shenzhen 518000, China (e-mail: chenzhm@pcl.ac.cn).

H. Y. Fu is with the Tsinghua-Berkeley Shenzhen Institute & Tsinghua Shenzhen International Graduate School, Tsinghua University, Shenzhen 518055, China, and also with the Southern Marine Science and Engineering Guangdong Laboratory, Zhuhai 519000, China (e-mail: hyfu@sz.tsinghua.edu.cn).

M. S. Aruna Gandhi and Qian Li are with the School of Electronics and Computer Engineering, Peking University, Shenzhen 518055, China (e-mail: aruna@pkusz.edu.cn; liqian@pkusz.edu.cn).

Digital Object Identifier 10.1109/JPHOT.2022.3179899

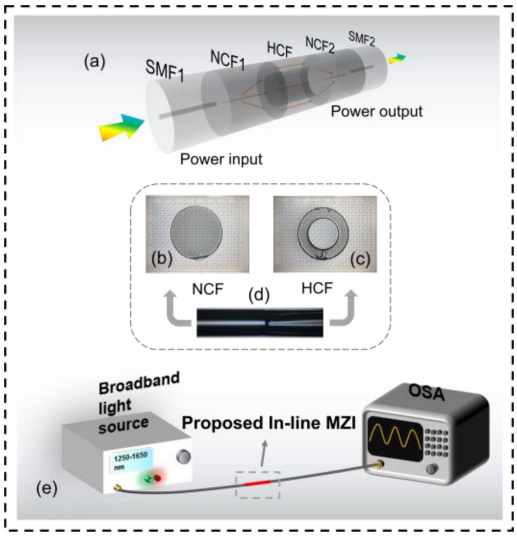

Fig. 1. (a) The schematic diagram of the NCF-HCF-NCF in-line MZI. (b) The microscopic image of the cross section of the NCF. (c) The microscopic image of the cross section of the HCF. (d) The microscopic image of the splicing point of the NCF (left) and the HCF (right). (e) The experimental setup, the proposed MZI is connected with the broadband light source and the optical spectrum analyzer.

torsion of the MZI are demonstrated. Combining with the compact structure, this MZI based on NCF-HCF-NCF structure is verified to be a stable and universal reference arm for high-quality Vernier effect generation, which improves the practicability of the PMF based fiber optic sensor with Vernier effect.

II. Sample Preparation and Principle

The schematic diagram of the NCF-HCF-NCF MZI is illustrated in Fig. 1(a), an HCF is sandwiched in two sections of NCFs. The structure is spliced with a lead-in single mode fiber 1 (G.652.D, YOFC, SMF1) and an output SMF2 in a transmissive link. Fig. 1(b) and (c) show the microscopic images of the cross sections of the NCFs (CL1010-A, YOFC) and the HCF (TSP075150, Polymicro). The core diameter of SMF is 9 μm, while there is no core/cladding structure within NCF. The inner and outer diameter of HCF is 75 μm and 125 μm, respectively. The microscopic image of the splice point of the NCF with the HCF is shown in Fig. 1(d).

The fabrication is under the fusion-cutting method. As is depicted in Fig. 2, the detailed process is as follow: firstly, the NCF is spliced with the lead-in SMF, then the fiber length of NCF1 is cut to be 1 mm, followed by a splicing between the HCF and the NCF1, and another splicing between the NCF2 and the HCF. The fiber length of the HCF is cut to be the designated (0.5, 1, 2, 3, and 4 mm) and the fiber length of the NCF2 is cut to be 1 mm as the same as NCF1. In this structure, NCF1 and NCF2 work as the beam splitter and beam combiner, respectively. Which is vital for the Mach-Zehnder interference. The light is transmitted in the HCF via core mode and wall mode. The core mode is propagated in the air-core, and the wall mode is confined and transmitted in the silica-wall of the HCF. The intensity of the transmission spectrum of the MZI can be

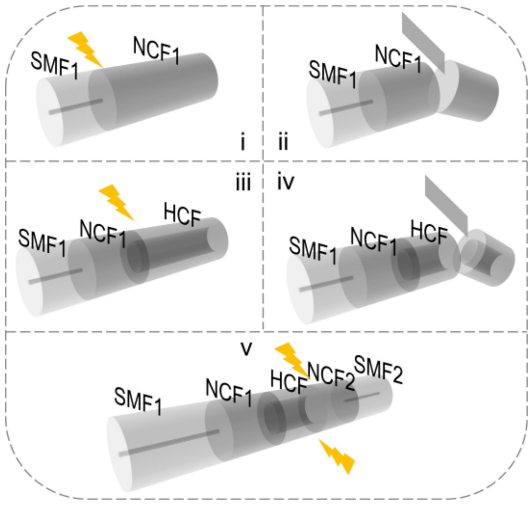

Fig. 2. The fabrication process by splicing-cutting method.

expressed as [23]

$$I = I_1 + I_2 + 2\sqrt{I_1 I_2}\cos(\Delta\phi), \tag{1}$$

where the I_1 and I_2 are the light intensity of the core mode and the wall mode, respectively. $\Delta\phi$ is the phase difference between the two modes, which can be described as

$$\Delta\phi = \frac{2\pi L}{\lambda}(n_2 - n_1), \tag{2}$$

where L is the length of the HCF, λ is the wavelength of incident light, n_1 and n_2 are the refractive indices of the core mode and the wall mode. The FSR of the interference spectrum can be then calculated as

$$FSR = \frac{\lambda_{\mathrm{m}}^2}{(n_2 - n_1)L}, \tag{3}$$

where λ_{m} is the wavelength of the m^{th} interference dip, m is an integer. Under temperature, strain, torsion and RI variations, the dip wavelength is shifted by the change of the phase difference. Next, the experiment is carried out to investigate the ambient dependence of the in-line MZI.

III. Experiments Results and Discussions

In order to analyze the spectral characteristics and the sensing performance of the in-line MZI, 5 samples with HCF lengths of 0.5 mm, 1 mm, 2 mm, 3 mm, and 4 mm are fabricated. The sensing experimental setup is shown in Fig. 1(e). The light from the broadband light source (BLS, ASE-EB-D-3-3-FC, Fiberlake) is launched into the in-line MZI, and the transmission signal is collected in the optical spectrum analyzer (OSA, AQ6370D, Yokogawa). The transmission spectra of the 5 samples are given in Fig. 3(a), (b), (c), (d) and (e). With the length of HCF increases from 0.5 mm to 4 mm, the FSR around 1450 nm decreases from 10.11 nm to 1.08 nm. The ER is calculated by taking the average value of 10 dips located around 1450 nm. The measured ERs are 20.08 dB, 19.26 dB, 20.07 dB, 19.27 dB and 20.22 dB, accordingly. It is verified that by modulating the length of HCF,

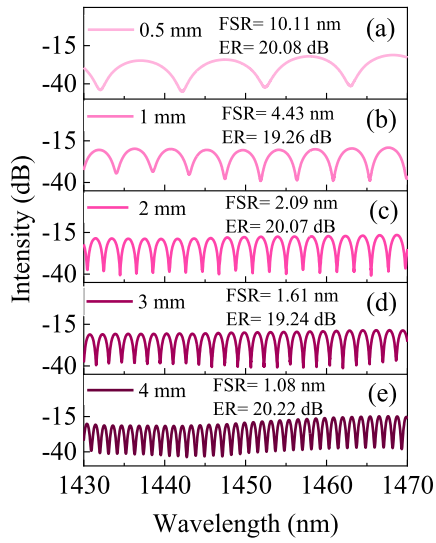

Fig. 3. The transmission spectra of the in-line MZI with the HCF length of (a) 0.5 mm, (b) 1 mm, (c) 2 mm, (d) 3 mm and (e) 4 mm.

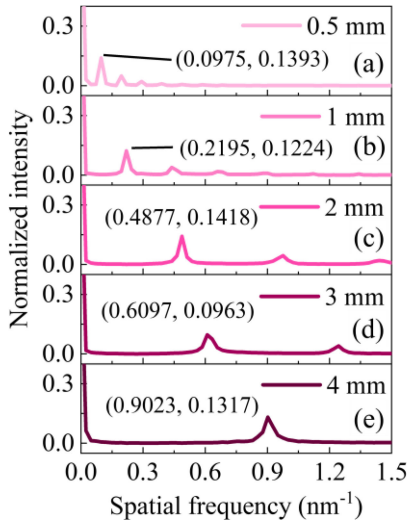

Fig. 4. The FFT spectra of the corresponding transmission spectra with the HCF length of (a) 0.5 mm, (b) 1 mm, (c) 2 mm, (d) 3 mm, and (e) 4 mm.

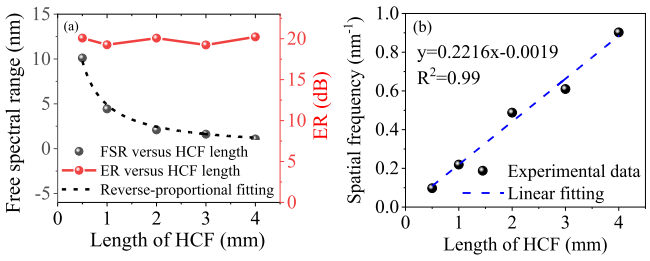

Fig. 5. (a) The relationship between the FSR (black, left y-axis) and the ER (red, right y-axis) with the length of HCF. (b) The relationship of the spatial frequency of the dominated peak and the length of HCF.

the FSR can be tuned in a large range, while the ER remains at a high value.

Fig. 5(a) shows the relationship between the FSR and the length of HCF, and the relationship between the ER and the length of HCF. The variation trends of FSR and ER with the increase of HCF length are distinctly depicted. For the 5 samples with different HCF lengths, the ER varies less than 1 dB. The relationship of FSR and HCF length is well depicted by a reverse-proportional fitting, which is accordant with (3).

The fast Fourier transform (FFT) algorithm is implemented to analyze the spatial frequency distribution of the transmission spectra. The FFT spectra of the in-line MZI with the HCF lengths of 0.5, 1, 2, 3 and 4 mm are provided in Fig. 4(a), (b), (c), (d) and (e), accordingly. There are two dominated peaks located in the spatial frequency domain. The spatial frequency located at 0 nm^{-1} is corresponding to the air-core mode, and another dominated peak corresponds to the silica-wall mode. The exact values of spatial frequency of the silica-wall mode are calculated, the spatial frequency shifts from 0.0975 nm^{-1} to 0.9023 nm^{-1} with the increase of the HCF length. The relationship between spatial frequency ξ and the length of HCF L can be expressed as [4]

$$\xi = \frac{(n_2 - n_1)}{\lambda^2} L. \tag{4}$$

In addition, the measured spatial frequency of the dominated peak versus the HCF length is plotted in Fig. 5(b). A linear fitting is carried out to depict the experimental results. The equation of the linear fitting is y = 0.2216x – 0.0019, with an R^2 of 0.99. From (4), the slope of the linear fitting can be used for calculating the effective RI difference of the two modes. The measured slope of the fitting curve is 0.2216 ± 0.015 (nm^{-1}/mm). Therefore, the effective RI difference can be calculated as 0.4659 ± 0.003 at around 1450 nm.

To demonstrate the feasibility of the in-line MZI employing as a reliable reference arm in Vernier effect sensing system, the ambient dependence needs to be investigated. For the temperature and the strain response, the data from Ref. [23] gives us a reference. For the achieved temperature sensitivity of ∼30.92 pm/ °C in a wide range of 30 – 90 °C, it is almost 53 times lower than that of the PMF based interferometer [13]. Therefore, when the in-line MZI works as the reference arm with the sensing arm of PMF based interferometer, the temperature crosstalk on the MZI can be neglected. In addition, a low strain response of ∼ 0.652 pm/$\mu\varepsilon$ in the range of 0 – 700 $\mu\varepsilon$ is achieved, which benefits from the robust structure. The strain sensitivity is nearly 20 times lower than that of the PMF based interferometer [24].

Owing to the existence of the NCF, the light can interact with ambient surrounding directly. Therefore, the environmental RI is supposed to influence the light transmission in the NCF. Furthermore, once under twisted conditions, the optical path difference of the two transmission modes in the HCF are varied. Therefore, the response of the MZI to ambient RI change and applied torsion are tested. The RI test is carried out by immersing

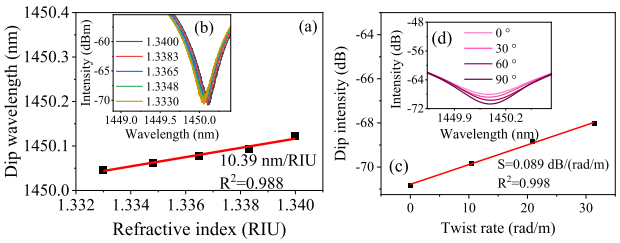

Fig. 6. (a) The RI response of the in-line MZI, inset (b) shows the dip wavelength shift when ambient RI changes from 1.333 to 1.3400. (c) The torsion response of the in-line MZI, inset (d) shows the dip intensity change when the torsion is applied on the device.

TABLE I
COMPARISON OF RI AND TORSION SENSING PERFORMANCE OF RELATED WORKS BASED ON HYBRID FUSION SPLICING STRUCTURE

Ref.	Type	RI sensitivity	Torsion sensitivity
[27]	NCF-LPG	141.837 nm/RIU	N/A
[28]	NCF-MZI	1800 nm/RIU	N/A
[29]	MMF-MZI	286.2 nm/RIU	N/A
[25]	Seven-core fiber-MZI	N/A	−400 pm/(rad/m)
[30]	Two-mode fiber-LPG	N/A	0.47 nm/(rad/m)
[31]	Ball-taper structure	N/A	0.089 nm/(rad/m)
This work	In-line MZI	10.39 nm/RIU	0.089 dB/(rad/m)

the device into alcohol solutions with the RI range of 1.3330 – 1.3400, with each step of about 0.0018 RI unit (RIU). The torsion test is also carried out by putting the device on the rotation stage and rotating the stages to different angles. The rotation ratio is calculated as the rotation angle per length. [25] Fig. 6(a) and (b) show the sensing response to ambient RI while Fig. 6(c) and (d) depict the spectral dependence on applied torsion. respectively. The proposed in-line MZI exhibits a sensitivity of 10.39 nm/RIU and a sensitivity of 0.089 dB/(rad/m), which shows the low spectral dependence to RI and torsion variation. Table I presents the RI and torsion sensing performance comparison of related works. The proposed MZI exhibits a low RI sensitivity is owing to that the NCF only works as the beam splitter and beam combiner, rather than the place where the interference occurs. In previous works with higher RI sensitivity [27], [28], the NCF is the core element where the phase modulated by ambient environment changes. For the low torsion sensitivity, it can be explained that the device owns good symmetry and robustness to against the twist. The applied torsion hardly influences the phase difference accumulation in the HCF area, but only influences the intensity of the wall mode and light coupling in the second NCF. Therefore, only the intensity of the interferometric dips is modulated.

In order to investigate the potential of the in-line MZI as a reference arm in Vernier effect-based sensing system, we inset the in-line MZI in a transmissive way to a PMF based SI. As a comparison, the schematic diagram of the traditional cascaded system consisting two SIs [13], [26] is presented in Fig. 7(a). The

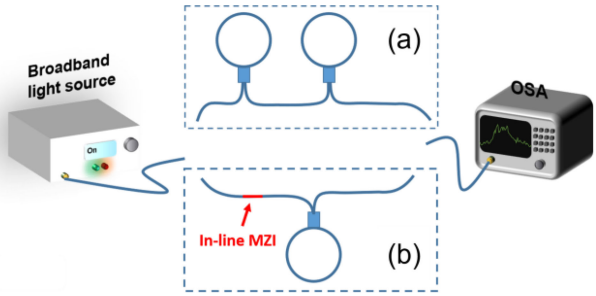

Fig. 7. Experimental setup comparison between the Vernier effect based sensing system consisting of (a) two cascaded PMF based SIs and (b) the PMF based SI with the in-line MZI inserted. The red line highlights the part of the compact in-line MZI.

schematic diagram of the cascaded system with proposed in-line MZI is shown in Fig. 7(b). The compact size of the in-line MZI is highlighted. HCF based FPI working as the reference arm is also compact [16], but the mismatch of the ER between the FPI and the SI will cause a lower ER of the superimposed envelope, which brings a lower measurement accuracy.

After cascaded with the Sagnac loop, the FSR of the superimposed spectrum $FSR_{envelope}$ can be calculated as

$$FSR_{envelope} = \frac{FSR_{MZI} \times FSR_{SI}}{|FSR_{MZI} - FSR_{SI}|}, \tag{5}$$

where FSR_{MZI} and FSR_{SI} are the FSRs of the proposed in-line MZI and the PMF based SI, respectively. After the two interferometers cascaded, the $FSR_{envelope}$ is magnified with a coefficient of M, which can be expressed as

$$M = \frac{FSR_{MZI}}{|FSR_{MZI} - FSR_{SI}|}. \tag{6}$$

When the PMF based SI experiences a wavelength shift $\Delta\lambda$ induced by ambient temperature changes, under the amplification of Vernier effect, the envelope dip of superimposed spectrum will experience a huge shift $\Delta\lambda_{envelope}$, which can be calculated as

$$\Delta\lambda_{envelope} = M \times \Delta\lambda. \tag{7}$$

Therefore, the temperature sensitivity of the PMF based SI can be remarkably enhanced. To show the Vernier spectra and the sensitivity enhancement characteristics, the temperature sensing experiment is conducted. Firstly, the dip wavelength shifts of single sensing arm SI with FSR of 2.20 nm, is recorded. When the temperature is changed from 30 °C to 30.5 °C in a high-resolution furnace (SNR-030H, Schneier), the dip wavelength of the single SI is blue-shifted 0.87 nm, as shown in Fig. 8(a) and (b), which is close to the reported sensitivity of PMF-SI [13]. Here, we use the temperature range of 0.5 °C to record the wavelength shift. If a broader temperature range is used, the dip wavelength shift will exceed the whole FSR of the SI, which will lead to a misleading estimation of shift direction. Then the sensing arm SI is cascaded with the in-line MZI with the HCF length of 2 mm, whose FSR is 2.09 nm. The Vernier spectrum under 30 °C is measured and presented in Fig. 8(c). For the superimposed spectrum, the upper envelope and the lower

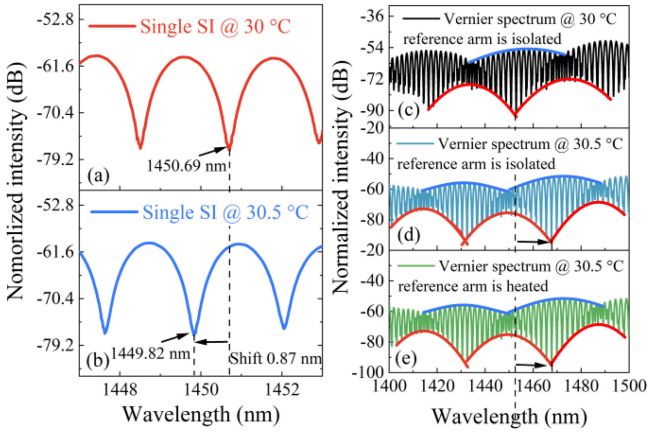

Fig. 8. (a) The interferometric spectrum of single SI sensing arm at the ambient temperature of 30 °C; (b) The dip wavelength of the SI interferometric spectrum blue shifts 0.87 nm when the ambient temperature increases to 30.5 °C; (c) The Vernier spectrum of the PMF-SI inserted with the proposed in-line MZI at 30 °C; The spectral shift of the Vernier system when reference arm is isolated (d) and heated (e) in the temperature range from 30 °C to 30.5 °C, respectively.

envelope are Gaussian-fitted to accurately track the peak or dip location and presented in blue and red curves, respectively. For the upper envelope, the ER can reach up to 9.02 dB. The ER of the lower envelope can be 18 dB, which are much higher compared to the works based on FPI [12], [14], shows the excellent ER match between the spectra of the MZI and that of the SI. The FSR of the Vernier envelope is 39.6 nm, which is very close to the theoretical value of 41.8 nm according to (5). The small difference might result from the measurement error. When the in-line MZI is cascaded with the SI, and under the condition that only the SI is put in the furnace, the spectral redshift of the Vernier spectrum is 16.88 nm, which is shown in Fig. 8(d). The sensitivity amplification is 19.4, which is close to the theoretical value of 19. Owing to the thermo-insensitivity of the MZI, when we put the reference arm in the furnace together with the sensing arm, the spectral shift is 16.40 nm, as shown in Fig. 8(e), which is very close to the condition that the reference arm is well isolated. The opposite shift direction compared to single arm can be explained by (6). The FSR of MZI is smaller than that of the SI, therefore, the denominator should be negative, which leads a opposite spectral shift. Therefore, the temperature insensitivity of the in-line MZI enables the Vernier effect to be applied in practical applications, where the isolation of reference arm is not needed. Note that, the experiment is to verify that the temperature sensing performance is hardly influenced by the circumstance of the in-line MZI reference arm. The Vernier effect amplification coefficient could be further improved by modulating the length of PMF easily to obtain higher value. Compared to the conditional configuration of two SIs, the reference arm made by the proposed MZI is more practical in real applications, which make the sensing system compact and reference arm isolation-free.

Therefore, the proposed in-line MZI can serve as a compact reference arm in the Vernier effect sensing system, especially

TABLE II
COMPARISON OF THE REFERENCE ARMS OF REPORTED PMF BASED VERNIER SENSING SYSTEMS

Ref.	Reference arm	Size	ER of envelope	Need of isolation
[10]	PMF based	Bulky (1.78 m)	High	Y
[13]	PMF based	Bulky (2.01 m)	High	Y
[12]	HCF based FPI	Middle (extra circulator)	Low	N
[14]	HCF based FPI	Compact	Low	N
This work	In-line MZI	Compact	High	N

cascaded with PMF based SIs. Here we present Table II to compare the related works of PMF based Vernier effect sensing system to show the superiority of our proposed MZI as the reference arm.

IV. CONCLUSION

In conclusion, a compact in-line MZI based on NCF-HCF-NCF structure is proposed as the reference arm for Vernier effect generation with high ER. The environmental insensitivities of the MZI to temperature, strain, RI and torsion enables it to work as the reference arm to amplify the sensitivity of the Vernier effect system. The ER of the transmission spectrum remains high regardless of the FSR change, which ensures the high ER of the Vernier spectrum when cascaded with SI. The compact size, environmental insensitivity and good spectral characteristics ensure the in-line MZI as an excellent reference arm to enhance the sensitivity of the Vernier effect sensing system in real applications.

REFERENCES

[1] X. Zhang *et al.*, "Angled fiber-based Fabry–Perot interferometer," *Opt. Lett.*, vol. 45, no. 2, pp. 292–295, 2020.
[2] W. Ni *et al.*, "Ultrathin graphene diaphragm-based extrinsic Fabry-Perot interferometer for ultra-wideband fiber optic acoustic sensing," *Opt. Exp.*, vol. 26, no. 16, pp. 20758–20767, 2018.
[3] M. Dai, Y. Zhao, Z. Chen, and H. Fu, "Fiber tip temperature sensor based on PVA filled silica tube Fabry-Perot interferometer," in *Proc. 12th Int. Conf. Adv. Infocomm Technol.*, 2020, pp. 19–22.
[4] S. Marrujo-García, I. Hernández-Romano, M. Torres-Cisneros, D. A. May-Arrioja, V. P. Minkovich, and D. Monzón-Hernández, "Temperature-independent curvature sensor based on in-fiber Mach–Zehnder interferometer using hollow-core fiber," *J. Lightw. Technol.*, vol. 38, no. 15, pp. 4166–4173, 2020.
[5] F. Ahmed, V. Ahsani, S. Jo, C. Bradley, E. Toyserkani, and M. B. G. Jun, "Measurement of in-fiber refractive index change using a Mach–Zehnder interferometer," *IEEE Photon. Technol. Lett.*, vol. 31, no. 1, pp. 74–77, Jan. 2019.
[6] M. Dai, Z. Chen, Y. Zhao, and H. Fu, "High performance in-line Mach-Zehnder interferometer as reference arm for vernier effect generation," in *Proc. Asia Commun. Photon. Conf.*, Optical Society of America, WA, DC, USA, 2021, pp. T4A.13.
[7] Z. Li, Y. X. Zhang, W. G. Zhang, L. X. Kong, Y. Yue, and T. Y. Yan, "Parallelized fiber Michelson interferometers with advanced curvature sensitivity plus abated temperature crosstalk," *Opt. Lett.*, vol. 45, no. 18, pp. 4996–4999, Sep. 2020.
[8] Y. Zhao *et al.*, "An integrated fiber michelson interferometer based on twin-core and side-hole fibers for multiparameter sensing," *J. Lightw. Technol.*, vol. 36, no. 4, pp. 993–997, Feb. 2018.

[9] R. Chu *et al.*, "All-optical graphene-oxide humidity sensor based on a side-polished symmetrical twin-core fiber Michelson interferometer," *Sensors Actuators B: Chem.*, vol. 284, pp. 623–627, 2019.
[10] H. Fu *et al.*, "Pressure sensor realized with polarization-maintaining photonic crystal fiber-based Sagnac interferometer," *Appl. Opt.*, vol. 47, no. 15, pp. 2835–2839, 2008.
[11] A. Starodumov, L. Zenteno, D. Monzon, and E. De La Rosa, "Fiber Sagnac interferometer temperature sensor," *Appl. Phys. Lett.*, vol. 70, no. 1, pp. 19–21, 1997.
[12] T. Claes, W. Bogaerts, and P. Bienstman, "Experimental characterization of a silicon photonic biosensor consisting of two cascaded ring resonators based on the Vernier-effect and introduction of a curve fitting method for an improved detection limit," *Opt. Exp.*, vol. 18, no. 22, pp. 22747–22761, 2010.
[13] L.-Y. Shao *et al.*, "Sensitivity-enhanced temperature sensor with cascaded fiber optic Sagnac interferometers based on Vernier-effect," *Opt. Commun.*, vol. 336, pp. 73–76, 2015.
[14] E. Xu *et al.*, "Ultrahigh-Q microwave photonic filter with Vernier effect and wavelength conversion in a cascaded pair of active loops," *Opt. Lett.*, vol. 35, no. 8, pp. 1242–1244, 2010.
[15] Y. Chang, B. Dong, Y. Ma, J. Wei, Z. Ren, and C. Lee, "Vernier effect-based tunable mid-infrared sensor using silicon-on-insulator cascaded rings," *Opt. Exp.*, vol. 28, no. 5, pp. 6251–6260, 2020.
[16] Y. Yang *et al.*, "Sensitivity-enhanced temperature sensor by hybrid cascaded configuration of a Sagnac loop and a FP cavity," *Opt. Exp.*, vol. 25, no. 26, pp. 33290–33296, 2017.
[17] Y. Zhao *et al.*, "Ultrasensitive temperature sensor with Vernier-effect improved fiber Michelson interferometer," *Opt. Exp.*, vol. 29, no. 2, pp. 1090–1101, 2021.
[18] B. Huang, Y. Wang, C. Liao, and Y. Wang, "Highly sensitive temperature sensor based on all-fiber polarization interference filter with Vernier effect," *IEEE Access*, vol. 8, pp. 207397–207403, 2020.
[19] Y. Zhao, Z.-R. Zhang, S.-C. Yan, and R.-J. Tong, "High-sensitivity temperature sensor based on reflective Solc-like filter with cascaded polarization maintaining fibers," *IEEE Trans. Instrum. Meas.*, vol. 70, 2021, Art no. 9509808.
[20] S. Liu, G. Lu, D. Lv, M. Chen, and Z. Zhang, "Sensitivity enhanced temperature sensor with cascaded Sagnac loops based on harmonic Vernier effect," *Opt. Fiber Technol.*, vol. 66, 2021, Art. no. 102654.
[21] G. Zhang *et al.*, "Ultra-sensitive high temperature sensor based on a PMPCF tip cascaded with an ECPMF Sagnac loop," *Sensors Actuators A: Phys.*, vol. 314, 2020, Art. no. 112219.
[22] X. Zhou, Y. Zhou, Z. Li, M. Bi, G. Yang, and T. Wang, "Research on temperature sensing characteristics with cascaded fiber Sagnac interferometer and fiber Fabry–Perot interferometer-based fiber laser," *Opt. Eng.*, vol. 58, no. 5, 2019, Art. no. 057103.
[23] Y. Wu, Y. Yang, W. Jin, Y. Shen, and S. Jian, "Compact Mach–Zehnder interferometer-based no-core fiber hollow-core fiber no-core fiber structure," *Opt. Eng.*, vol. 56, no. 3, 2017, Art. no. 030501.
[24] P. M. R. Robalinho, A. D. Gomes, and O. Frazao, "High enhancement strain sensor based on Vernier effect using 2-Fiber loop mirrors," *IEEE Photon. Technol. Lett.*, vol. 32, no. 18, pp. 1139–1142, Sep. 2020.
[25] C. Liu *et al.*, "Strain-insensitive twist and temperature sensor based on seven-core fiber," *Sensors Actuators A: Phys.*, vol. 290, pp. 172–176, 2019.
[26] Z. Ding, Z. Tan, P. Zhang, and L. Zhang, "Highly sensitive temperature sensor based on cascaded HiBi-FLMs with the Vernier effect," *J. Opt. Soc. Amer.: B*, vol. 37, no. 7, pp. 1948–1955, 2020.
[27] T. Geng *et al.*, "A temperature-insensitive refractive index sensor based on no-core fiber embedded long period grating," *J. Lightw. Technol.*, vol. 35, no. 24, pp. 5391–5396, 2017.
[28] S. Silva *et al.*, "Ultrahigh-sensitivity temperature fiber sensor based on multimode interference," *Appl. Opt.*, vol. 51, no. 16, pp. 3236–3242, 2012.
[29] Y. Zhao *et al.*, "Investigation of the high sensitivity RI sensor based on SMS fiber structure," *Sensors Actuators A: Phys.*, vol. 205, pp. 186–190, 2014.
[30] L. Zhang *et al.*, "High sensitivity twist sensor based on helical long-period grating written in two-mode fiber," *IEEE Photon. Technol. Lett.*, vol. 28, no. 15, pp. 1629–1632, Aug. 2016.
[31] S. Duan *et al.*, "High sensitive directional twist sensor based on a Mach–Zehnder interferometer," *IEEE Photon. J.*, vol. 10, no. 6, Dec. 2018, Art. no. 6804207.